RESEARCH ARTICLE
ATMOSPHERIC PHYSICS

Earth and Planetary Physics
10: 176–185, 2026
doi: 10.26464/epp2026002

Comparison of atmospheric gravity wave event statistics between Dandong and Lhasa

YiXuan Chen[1], Chang Lai[1,2*], QinZeng Li[2], JiYao Xu[2], and Wei Yuan[2]

[1]School of Science, University of Posts and Telecommunications of Chongqing, Chongqing 400065, China;

[2]State Key Laboratory of Space Weather, National Space Science Center, Chinese Academy of Sciences, Beijing 100190, China

Key Points:

- The atmospheric gravity wave data at Dandong and Lhasa were collected and statistically analyzed over a 3-year period from 2015 to 2017 through machine learning.
- Wind field-filtering effects were found to significantly influence the seasonal propagation trend.
- The wave sources and their influence on the direction of wave propagation were analyzed using the ray-tracing method.

Citation: Chen, Y. X., Lai, C., Li, Q. Z., Xu, J. Y., and Yuan, W. (2026). Comparison of atmospheric gravity wave event statistics between Dandong and Lhasa. *Earth Planet. Phys.*, *10*(1), 176–185. http://doi.org/10.26464/epp2026002

Abstract: Using a recognition model of atmospheric gravity waves (AGWs), we identified 519 AGW events from the OH airglow images observed at the Dandong and Lhasa stations from 2015 to 2017. The 317 AGW events detected at the Dandong station have wavelengths ranging from 30 to 60 km, periods from 14 to 20 min, horizontal speeds from 30 to 60 m/s, and relative intensities from 0.4% to 0.6%, respectively. The parameters of 202 events recorded at the Lhasa station mainly vary within 15–35 km in horizontal wavelength, 4–6 min in period, 40–100 m/s in horizontal velocity, and 0.1%–0.3% in relative intensity. The occurrence rate peaks in winter and summer at Dandong and the peak in summer are absent at Lhasa because of the lack of convective weather. The seasonal propagation directions of the waves are influenced by both the wind field-filtering effect and the distribution of wave sources. In spring, because of the southeastward background wind field, fewer southeastward events are observed at the Dandong station. The situation at the Lhasa station is similar. In summer, both the Lhasa and Dandong stations are dominated by northeastward AGWs, which can be attributed to the southwestward wind. In autumn, ray-tracing results show that the events at Dandong mainly originate from wind shear, whereas the events at the Lhasa station are triggered by convective weather. The location of the wave sources determines the trend of the propagation directions at the Dandong and Lhasa stations in autumn. In winter, because of the eastward wind, more events are propagating to the southwest at the Dandong station.

Keywords: atmospheric gravity waves; backward ray-tracing method; wind field filtering; convective precipitation

1. Introduction

In the troposphere, atmospheric gravity waves (AGWs) can be triggered by various factors, including the terrain (Jiang JH et al., 2002; Alexander and Teitelbaum, 2011), vertical wind shear (Clemesha and Batista, 2008; Nath and Chen W, 2013; Wang Y et al., 2019), a tsunami (Li QZ et al., 2024), convection (Kalisch et al., 2016; Bramberger et al., 2017; Jana et al., 2020), and jets and fronts (Fritts and Luo ZG, 1992; Luo ZG and Fritts, 1993). These waves propagate upward, transferring momentum and energy to the mesosphere and lower thermosphere (MLT), thereby significantly influencing atmospheric circulation (Fritts and Alexander, 2003). When AGWs propagate to the OH airglow layer at approximately 87 km altitude, the wave fluctuations induce perturbations in the airglow layer, which can be detected optically by all-sky airglow imagers (ASAIs; Garcia et al., 1997; Taylor, 1997). Observational studies have shown that AGWs are significantly influenced by the background winds in the middle atmosphere during their upward propagation (Medeiros et al., 2003; Triplett et al., 2017; Giongo et al., 2020). Taylor et al. (1993) observed in OH airglow images from Colorado (40°N, 105.6°W) that AGWs exhibited a pronounced preference for northward propagation, which was associated with the filtering effect of background winds.

Using airglow observation data, many researchers have conducted extensive statistical analyses of AGWs. Li QZ et al. (2018) utilized data from OH ASAIs located in Kazan, Russia (55.8°N, 49.2°E), to study mesospheric AGWs over four seasons from August 2015 to July 2016. They found that convection may be an important source of AGWs at higher latitudes. Wrasse et al. (2024) conducted a 5-year statistical analysis of AGWs by using the OH airglow imager located at São Martinho da Serra (29.44°S, 53.82°W) in southern Brazil and found that the propagation direction of AGWs exhibits substantial seasonal dependence, primarily propagating southeast during the summer and autumn seasons. Throughout 11 months, Suzuki et al. (2004) used airglow images

First author: Y. X. Chen, s220601004@stu.cqupt.edu.cn
Correspondence to: C. Lai, laichang@cqupt.edu.cn
Received 14 FEB 2025; Accepted 22 SEP 2025.
First Published online 30 SEP 2025.

observed by the airglow imager assigned in Darwin, Australia (12.4°S, 131.0°E), to investigate the wavelengths, phase velocities, and propagation directions of AGWs; they discovered that the propagation directions are closely related to the seasons. Cao B and Liu AZ (2022) suggested that the preferred wave propagation direction and frequency of occurrence are closely related to nearby convective activities at the Andes Lidar Observatory (ALO, 30.3°S, 70.7°W) in northern Chile, particularly during the solstice season. However, statistical comparative analyses of AGWs in regions with substantially different geographical environments remain insufficient, and the effects of orography and climate, such as monsoonal dynamics and severe convective systems, on the generation and propagation of AGWs have not yet been clearly revealed.

The Chinese Meridian Project has established multiple airglow observation stations across China (Xu JY et al., 2015), which have accumulated a substantial amount of airglow data from various regions. The Lhasa station (30.1°N, 90.5°E), located in the southeastern part of the Tibetan Plateau, features a unique geographical and climatic environment that strongly affects the global climate (Li QZ et al., 2016; Fu YF et al., 2020). The Dandong station (40.0°N, 124.0°E), situated in northeast China near the Yellow Sea, has different geographical and climatic characteristics from the Lhasa station. Using previously trained machine learning models (Lai C et al., 2019), we extracted the parameters of AGWs from OH airglow data at the Lhasa and Dandong sites for the period from 2015 to 2017. From a comparison of the AGW parameters from the two sites, we discuss the influence of local climatic conditions on the generation and propagation of AGWs.

The structure of this paper is as follows: Section 2 provides a brief introduction to the observation and data processing; Section 3 presents a statistical analysis of the AGW parameters and analyses the AGW sources when using the backward ray-tracing method, along with wind data and convective precipitation fields from the European Centre for Medium-Range Weather Forecasts (ECMWF); and Section 4 presents the conclusions.

2. Observation and Data Analysis

2.1 Airglow Imager

The ASAI systems provide 180° full-sky coverage, with spatial resolution demonstrating substantial angular dependence: the maximum at the zenith (approximately 0.27 km) and gradually decreasing with an increasing observation angle. Considering the pronounced resolution degradation and optical distortion effects at the edge of the field of view, we limit the effective observation area in this study to within a 160° zenith angle. For quantitative analysis, the original images are geographically projected to a 512 × 512 km rectangular area, with subsequent processing conducted at a spatial resolution of 1 km/pixel. The temporal uncertainty is 64 s, including exposure and storage time. The near-infrared filter of the ASAI features a bandpass range of 715–930 nm with a notch at 865.5 nm to filter out O_2 emissions (Xu JY et al., 2015).

2.2 Processing of Airglow Data and Sources of Atmospheric Background Fields

The raw airglow images are processed according to the conventional method. The raw airglow images are first aligned to geographic north, followed by star removal to eliminate interference from starlight. The starless images are then projected onto a 512 × 512 geographic coordinate system (Li Q et al., 2011). Last, adjacent images are subtracted to reduce the background noise.

The machine learning-based program we previously developed (Lai C et al., 2019) was applied to extract valid AGW data from airglow images. The automatic detection of AGWs includes three steps. In the first step, raw images are categorized by a convolutional neural network (CNN) classification model with 99% accuracy (Lin ZS et al., 2023) to select images captured on clear (moonless starry) nights, which are suitable for observation. In the second step, AGWs are recognized and positioned from the unwarped airglow images taken on clear nights by using a detection model based on Faster Regional CNN (Faster R-CNN). In the last step, the parameters of the AGWs, such as horizontal wavelength, horizontal speed, observed period, and propagation direction, are extracted from the local area containing wave patterns by using a two-dimensional fast Fourier transform. A higher identification threshold was utilized in the automatic detection to minimize false positives. This conservative approach may have excluded some images with weaker wave signals at the beginning and end of an event, potentially leading to a modest underestimation of the occurrence rate. However, statistical comparisons confirm that this systematic error does not compromise the reliability of the AGW trend analyses.

The wind and temperature fields from the Modern-Era Retrospective analysis for Research and Applications, Version 2 (MERRA-2) dataset were used during the ray-tracing process in this study. MERRA-2 provides a horizontal resolution of 0.5° latitude × 0.625° longitude and a temporal resolution of 3 h, and it includes 72 pressure-based vertical levels, extending up to an altitude corresponding to 0.01 hPa. For the analysis, monthly mean wind and precipitation data from the fifth-generation ECMWF atmospheric reanalysis of the global climate (ERA-5) reanalysis dataset provided by the ECMWF were used. These data have a spatial resolution of 0.25° and include 37 vertical levels. In addition, precipitation data with a temporal resolution of 1 h were utilized to validate individual AGW events.

2.3 Ray-Tracing Method

In this study, we adopt a backward ray-tracing methodology based on the theoretical framework of Marks and Eckermann (1995) to inversely track the propagation paths of AGWs originating from an altitude of 87 km. The comprehensive gravity wave-tracing model was established by using critical parameters acquired from ASAI observations as initial inputs, which included the horizontal wavelength, propagation direction, horizontal phase velocity, observation period, and observation time.

For atmospheric data below 70 km altitude, background wind fields and temperature profiles were obtained from MERRA-2 reanalysis datasets. Atmospheric parameters above 70 km were derived from the 2014 Horizontal Wind Model (HWM-14) and Naval Research Laboratory Mass Spectrometer and Incoherent Scatter Radar Exosphere–2000 (NRLMSISE-00) empirical atmospheric model (Picone et al., 2002), respectively. The three-dimensional group velocity components—zonal (C_{gx}), meridional (C_{gy}), and vertical (C_{gz})—were determined by the following formulations:

$$C_{gx} = \frac{dx}{dt} = \frac{k_x(N^2 - \hat{\omega}^2)}{\hat{\omega}\Delta} + U, \tag{1}$$

$$C_{gy} = \frac{dy}{dt} = \frac{k_y(N^2 - \hat{\omega}^2)}{\hat{\omega}\Delta} + V, \tag{2}$$

$$C_{gz} = \frac{dz}{dt} = -\frac{m(\hat{\omega}^2 - f^2)}{\hat{\omega}\Delta}, \tag{3}$$

where k_x and k_y denote the zonal and meridional wavenumbers respectively, $\hat{\omega}$ represents the intrinsic frequency, and ω indicates the observed frequency. In addition, U and V correspond to the zonal and meridional wind speeds:

$$\hat{\omega} = \omega - k_x U - k_y V. \tag{4}$$

In Equation (3), Δ can be expressed as

$$\Delta = k_x^2 + k_y^2 + m^2 + \alpha^2, \tag{5}$$

$$\alpha^2 = \frac{1}{4h^2}, \tag{6}$$

where h denotes the density scale height (taken as 7 km in this study) and m represents the vertical wavenumber of the wave packet, which can be expressed as

$$m^2 = \frac{(k^2 + f^2)(N^2 - \hat{\omega}^2)}{\hat{\omega}^2 - f^2}. \tag{7}$$

In addition, N is the Brunt–Väisälä frequency and f is the Coriolis frequency. The backward trajectories were calculated with a time step of 100 m/C_{gz}. The ray-tracing process will stop when the vertical wave number m reaches any of the following conditions: (1) $m^2 < 0$, indicating wave reflection where AGWs cannot propagate vertically; (2) $m^2 > 1 \times 10^{-6}$ cyc^2/m^2, indicating AGWs approaching the critical layer with vertical wavelengths less than 1 km; (3) $|m| \to \infty$, where the AGW packet is breaking (Wrasse et al., 2006). The terminal of the tracing process is regarded as the probable source region of the AGW event.

3. Results and Discussion

3.1 Wave Parameter Statistics

From 979,743 airglow images captured between 2015 and 2017, 317 AGW events were detected at the Dandong station, and 202 AGW events were detected at the Lhasa station. The effective observation duration indicates the time of clear nights, when potential AGWs can be observed. The occurrence rate was defined as the duration time of AGW events divided by the effective observation duration time. Figure 1 illustrates the monthly average observation duration time, event duration time, and occurrence rate of the two stations. At the Dandong station, a large peak appears in the occurrence rate during the summer (May to August) and a smaller peak appears during the winter (November to February), which is similar to the stations at similar latitudes, such as Xinglong in China (40.2°N, 117.4°E) and Mt. Bohyun in Korea (36.2°N, 128.9°E; Kim et al., 2010; Li Q et al., 2011). However, the occurrence rate at Lhasa is low in summer and has only one peak in winter.

Figure 2 shows the distributions of wavelength, period, and relative intensity observed at the Dandong and Lhasa sites. At Dandong, the horizontal wavelengths are mainly distributed between 30.0 ± 1.8 and 60.0 ± 1.8 km, whereas at Lhasa, they are concentrated between 15.0 ± 1.0 and 35.0 ± 1.3 km, with average values of 43.7 km and 24.9 km, respectively. The observed periods are mostly in the range of 14.0 ± 1.3 and 20.0 ± 1.9 min at Dandong and 4 ± 1.0 and 6 ± 1.0 min at Lhasa. The relative intensities of AGWs are primarily concentrated within 0.4%–0.6% at Dandong and 0.1%–0.3% at Lhasa. These substantial differences in wave parameters suggest that the primary sources of AGW events at the two sites may differ from each other. The relative intensity I_r is calculated as

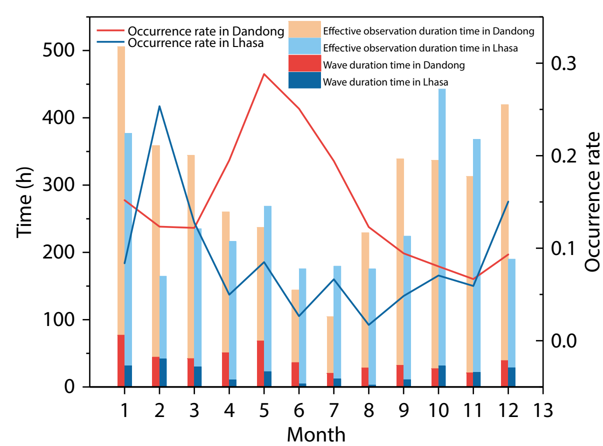

Figure 1. Monthly histogram of effective observations and wave durations. The red and deep blue bars are subsets of the orange and light blue bars.

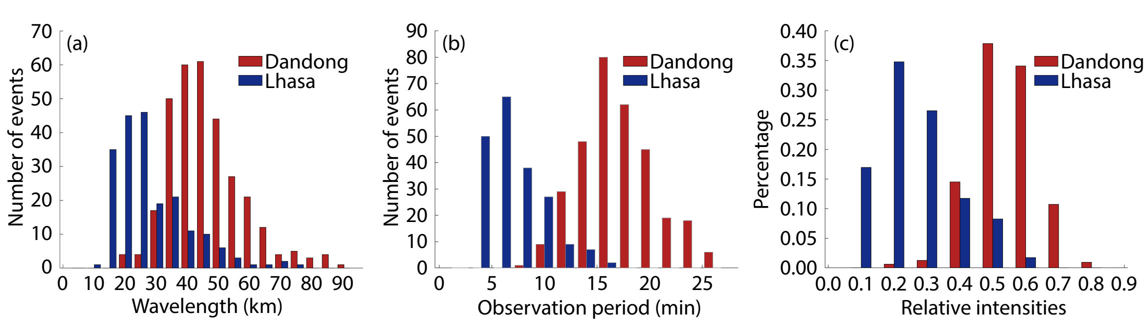

Figure 2. Distributions of gravity wave parameters: (a) wavelength, (b) observed period, (c) relative intensity.

$$I_r = \frac{I_{max} - I_{min}}{2I_{avg}}, \quad (8)$$

where I_{avg}, I_{max}, and I_{min} are the average, maximum, and minimum grayscale values of the detected wave-containing region.

3.2 Propagation Direction

Figure 3 shows the horizontal velocities of various AGW events in different seasons at Dandong and Lhasa, respectively. Figure 4 shows the monthly averaged wind field data (2015–2017) for Dandong and Lhasa, including MERRA-2 (0–70 km) and HWM-14 (55–87 km) data (Hedin et al., 1996; Rienecker et al., 2011). The data from MERRA-2 and HWM-14 were averaged for the 55–70 km overlapped range. During the upward propagation of AGWs, the background wind field plays a crucial role in modulating wave behavior. A wind field aligned with the wave propagation direction can enhance energy dissipation and potentially lead to wave breaking, especially when the background wind speed matches the horizontal phase speed of the wave. This condition defines the critical level, where wave energy is absorbed or dissipated. However, waves may still propagate upward even if their phase speed is slower than the background wind, as long as it does not match the wind speed. Propagation can also be maintained if the wave travels against the wind or if its phase speed exceeds the background wind speed. These wind-filtering effects may account for some of the observed statistical characteristics. In spring, the southeastward events at Dandong are 8.6% of the total, which can be attributed to the 50–100 m/s eastward wind and 20–30 m/s southward wind at approximately 10 km altitude. The observed five southeastward-propagating AGW events have horizontal speeds greater than 50 m/s. The situation at Lhasa during spring is almost the same, only one southeastward event (5.9%) spotted. In summer, 67.4% (62 cases) of events in Dandong and 68.9% (31 cases) in Lhasa propagated northeastward, with 95% confidence intervals (CIs) of 17.8°–45.6° and 10.3°–63.3°, respectively. This predominant northeastward propagation trend during the summer aligns with the observations at the Yucca Ridge Field Station near Fort Collins, Colorado (40.7°N, 104.9°W), and at São João do Cariri, Brazil (7°S, 36°W; Medeiros et al., 2004; Dou XK et al., 2010). The strong westward wind above 40 km and the southward wind at approximately 60 km are the reasons for the concentrated propagation direction. In autumn, 50.0% of the AGWs propagating over Dandong are northwestward, with 95% CIs of 281.3°–3.9°. Whereas in Lhasa, the wave propagation is mainly in the northeast (32.0%) and northwest (36.0%) directions, with 95% CIs of 300.2°–21.7°. These characteristics cannot be explained by the northeast wind field in Dandong and the east wind in Lhasa. In winter, there are 53.7% (66 cases) southwestward-propagating events above the Dandong station, with 95% CIs of 196.4°–230.1° because of the eastward winds at 10–20 km and northward wind at 70–80 km. However, 77.8% of events over Lhasa propagate toward northeast and southeast, with 95% CIs of 71.1°–118.8°, which cannot be explained by the eastward background wind field.

In this subsection, we analyzed the seasonal propagation trend of AGW events at Dandong and Lhasa in combination with the background wind fields. The wind field-filtering effect can explain the propagation characteristics in most cases. However, the autumn in both locations and the winter in Lhasa may be affected by factors beyond the wind field, suggesting a probable linkage to source distribution patterns.

3.3 Ray Tracing of an AGW Event

To verify the tropospheric origin of the wave, a case study was conducted on the gravity wave event observed at 16:53 UTC on

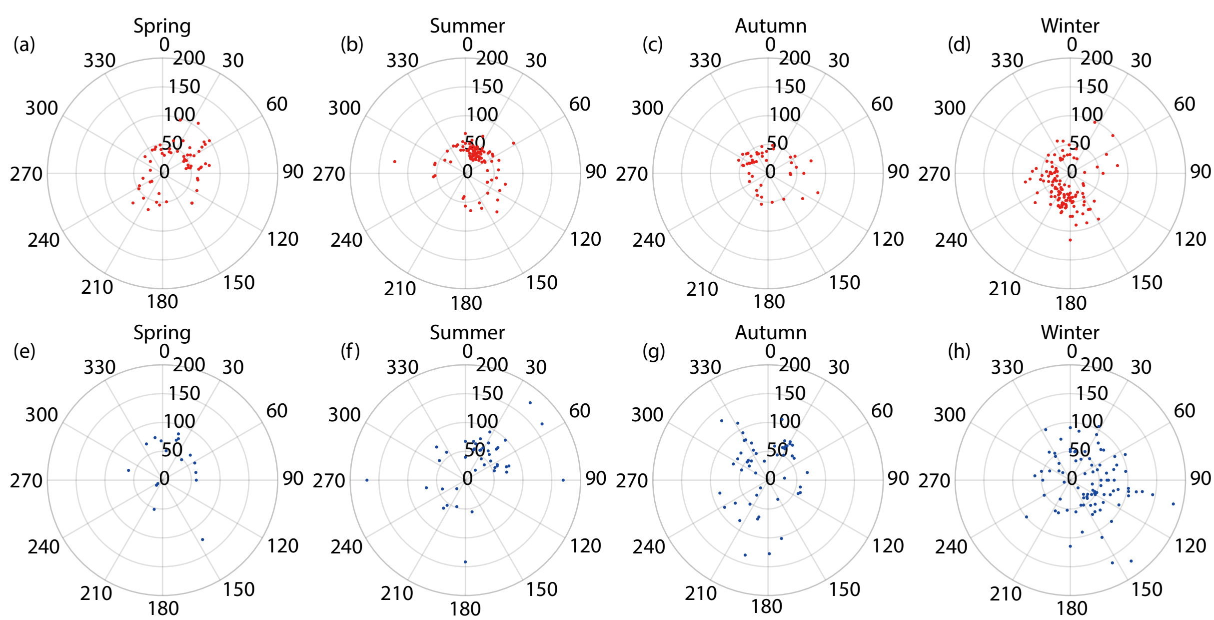

Figure 3. Seasonal propagation directions at Dandong (red dots) and Lhasa (blue dots) during different seasons: spring (March–April), summer (May–August), autumn (September–October), and winter (November–February). The radius represents the horizontal velocity, with an azimuth angle of 0° indicating the direction of geographic north.

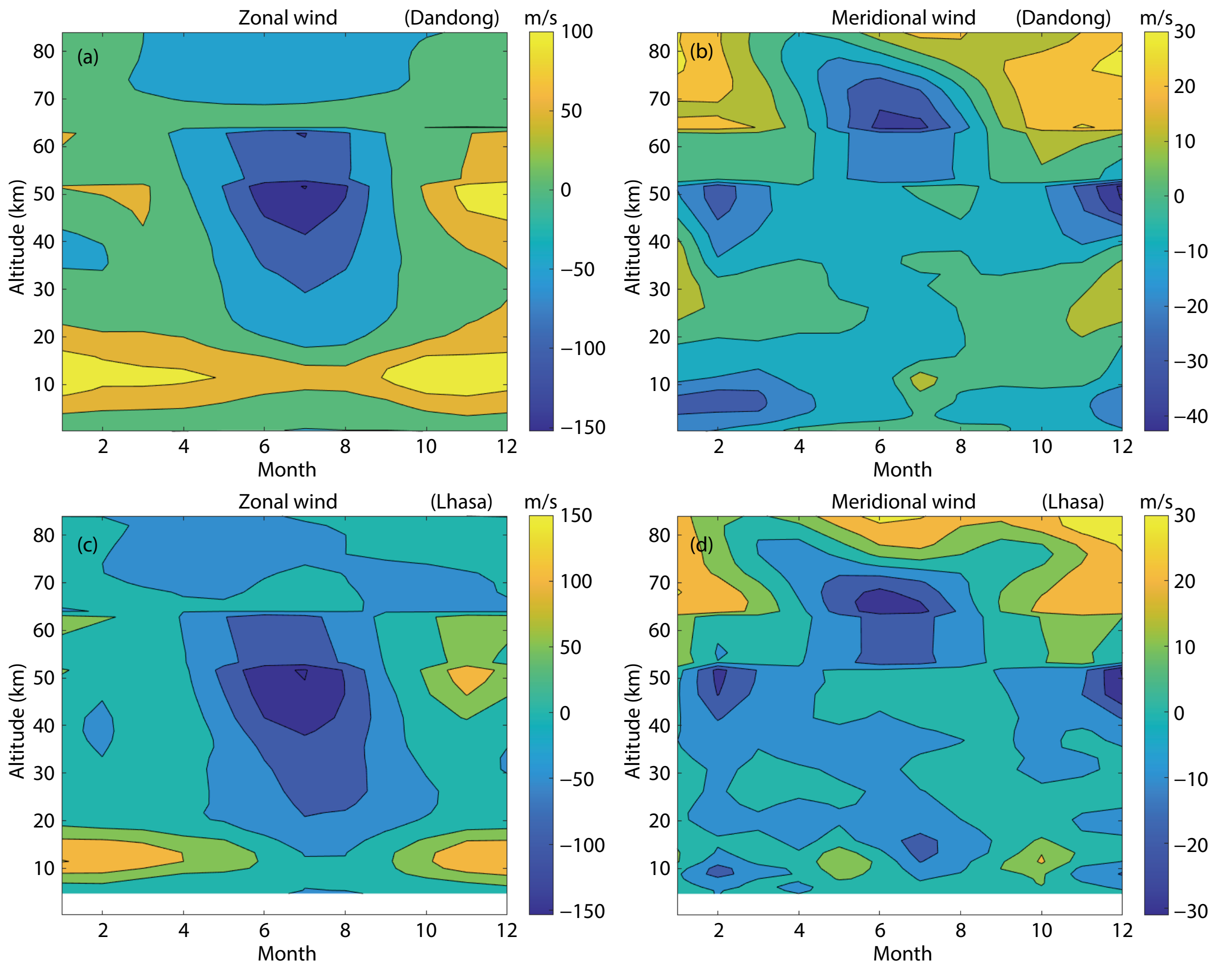

Figure 4. Monthly averaged wind field. (a, b) Average zonal and meridional wind variations at Dandong; (c, d) average zonal and meridional wind variations at Lhasa. Lhasa is at an altitude of 4 km; thus, no wind field data are below 4 km.

June 17, 2015, over the Dandong station. The wave propagated at azimuth 37° ± 3° with a horizontal wavelength of 34.9 ± 1.4 km, an observed period of 20.5 ± 1.3 min, a horizontal phase speed of approximately 30.0 ± 1.9 m/s, and a relative intensity of 0.465 ± 0.019.

Figures 5a, 5b, and 5c present the background atmospheric data used in the analysis. Figures 5d and 5e show the vertical profiles of the intrinsic frequency and Brunt–Väisälä frequency, calculated based on the observed wave parameters and background atmospheric conditions. The ray-tracing process terminated at an altitude of 10.6 km because of negative m^2. According to the back-traced result from the termination location (see Figures 6b and 6c) and zonal and meridional group velocities (Figure 6a), the estimated source is located at 123.09°E, 40.15°N. When we combine the estimated source with the convective precipitation distribution from ERA-5 reanalysis data at 16:00 UTC on June 17, 2015 (Figure 6d), we find a deep convective region near the inferred source location, indicating that this AGW event was most likely triggered by deep convection.

3.4 Sources of AGWs

The backward ray-tracing method, based on a three-dimensional nonhydrostatic ray-tracing model, was used to analyze the source regions of AGWs observed at Dandong and Lhasa, with the tracing initiated from an altitude of 87 km. As shown in Figure 7, approximately 63% of the 199 wave events observed at Dandong can be traced to altitudes below 13 km, whereas only approximately 20% of the 43 events observed at Lhasa can be traced to below 13 km. The 13 km altitude corresponds to the tropopause and lower stratosphere in most regions of China. Potential wave sources, such as topography, wind fields, and weather systems, are predominantly located within the troposphere. Although AGW sources may occur at any position along the path, most are thought to originate in the troposphere because of the stability of the stratosphere (Wrasse et al., 2006; Li QZ et al., 2016). The number of events traceable to below 13 km in Dandong and Lhasa during spring, summer, autumn, and winter are 44 and 5, 70 and 16, 27 and 12, and 58 and 8, respectively.

Convection weather and wind shear are candidate sources of local AGW events. Figure 8 demonstrates the monthly mean convective precipitation (average daily convective precipitation in a local area for a month) of four seasons from ERA-5 data. Figure 9 shows the average vertical wind shear intensity below 13 km over Lhasa and Dandong, derived from the ERA-5 zonal and meridional wind data. The sources traced to below 13 km are marked on the maps, and the red stars indicate the ASAI spots. The calculation is shown

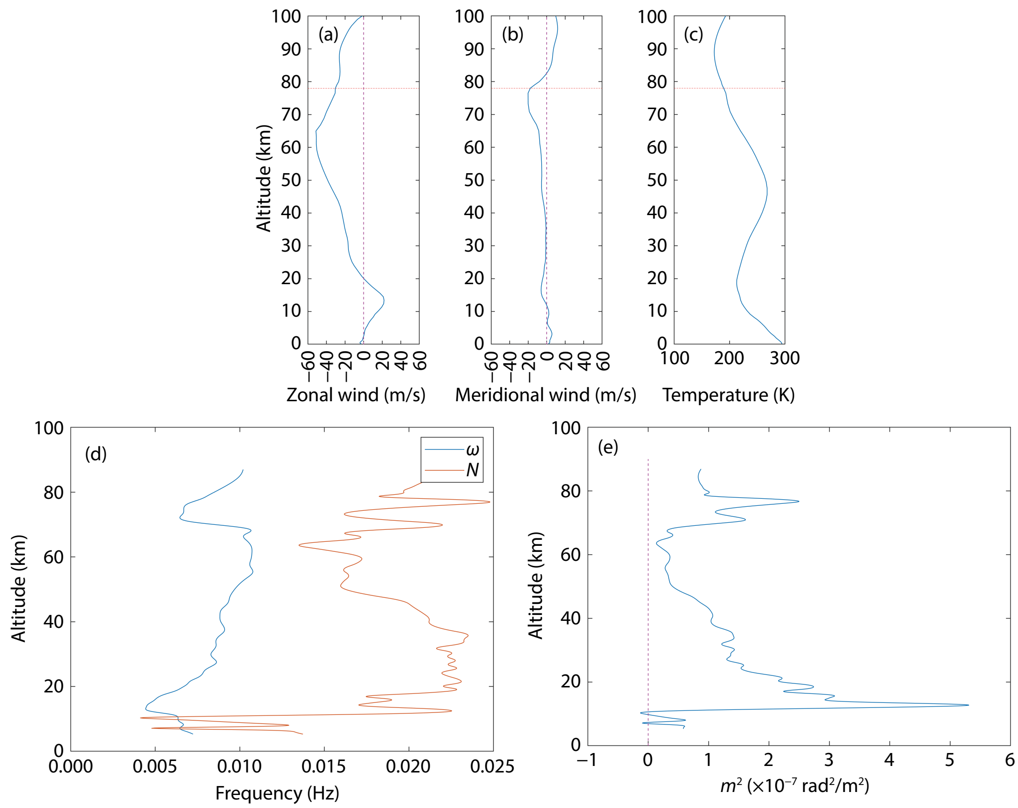

Figure 5. Profiles of the (a) zonal wind, (b) meridional wind, and (c) temperature. Above the dashed line, wind data are taken from the HWM-14 model and temperature data from the NRLMSISE-00 model; below the dashed line, MERRA-2 reanalysis data are used. Panel (d) displays the intrinsic frequency ω (blue line) and Brunt–Väisälä frequency N (red line), whereas panel (e) shows the corresponding squared vertical wavenumber.

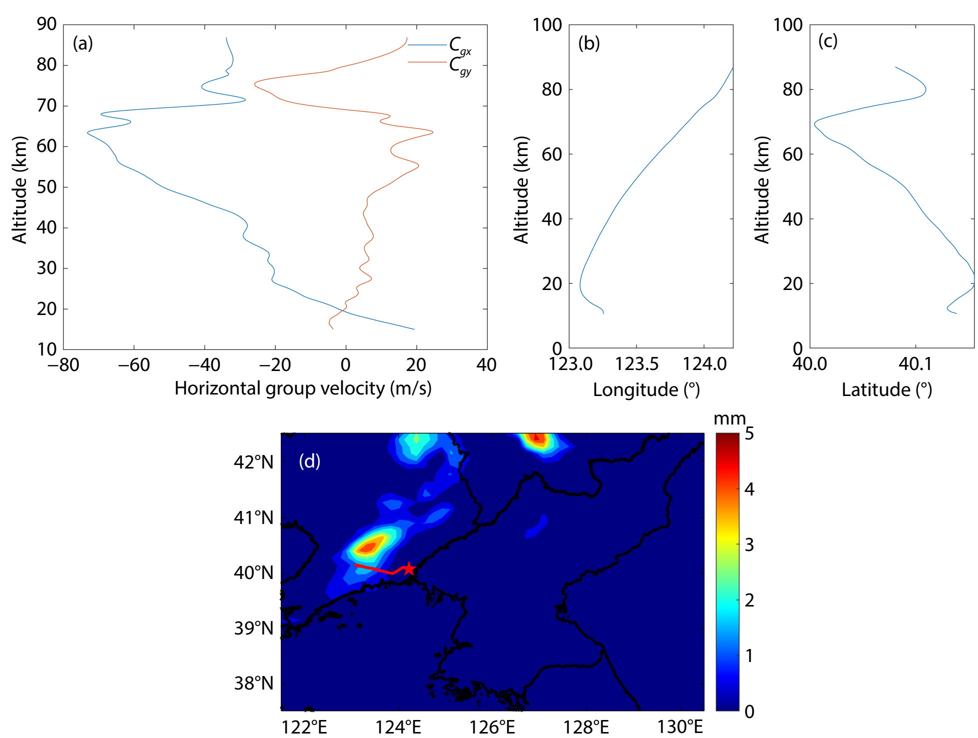

Figure 6. The result of the ray-tracing analysis: (a) zonal and meridional group velocities; (b, c) ray paths in the longitude and latitude, respectively; (d) convective precipitation from the ERA-5 reanalysis at 16:00 UTC on June 17, 2015. The red line indicates the traced path of the AGW, and the star marks the starting point of the backward tracing.

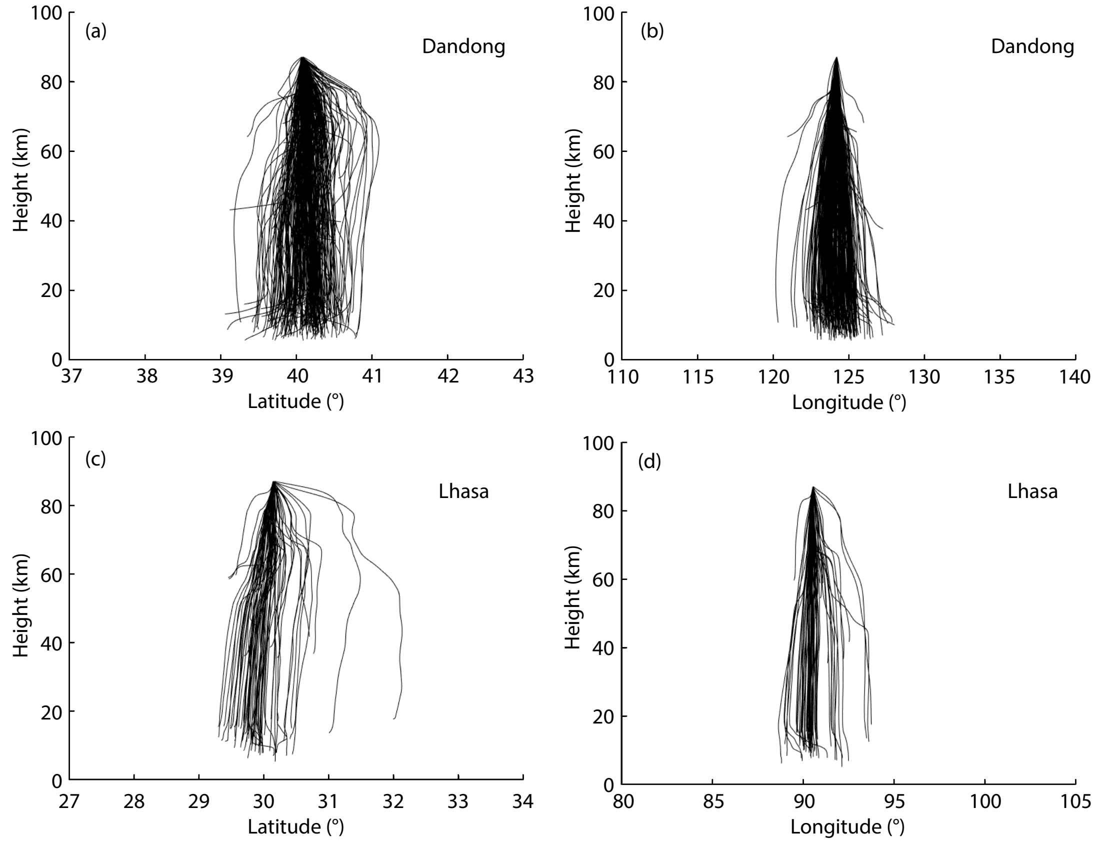

Figure 7. Ray-tracing results for Dandong (a, b) and Lhasa (c, d).

in Equation (9), where S represents the magnitude of the vertical wind shear:

$$S = \frac{\sqrt{(u_{200} - u_{850})^2 + (v_{200} - v_{850})^2}}{z_{200} - z_{850}}. \quad (9)$$

Here, u_{850} and u_{200} denote the zonal wind speed averages at the 850 and 200 hPa pressure levels, respectively, whereas v_{850} and v_{200} represent the meridional wind speed averages at the same levels. The z_{850} and z_{200} correspond to the altitudes of the 850 and 200 hPa pressure levels, which are approximately 2 and 13 km, respectively. In summer, convection is supposed to trigger most local AGW events because the convective rainfall is substantial whereas the wind shear is small. As shown in Figures 8b and 8f, the wave sources are distributed to the west of the ASAI spots and near the areas with higher precipitation, which is consistent with the northwestward propagation of the observed events. Meanwhile, strong westward winds at altitudes of 20–60 km filter out most of the westward-propagating AGWs generated by convective sources in the high precipitation area east of the spots. In autumn, 88.9% wave sources of traceable AGW events can be traced back to the east and southeast of Dandong, where the vertical wind shear is large (Figure 9c). At Lhasa, 66.6% of the wave sources are distributed to the southwest and southeast of the station, in the area of low vertical wind shear but with a certain amount of convective rainfall (Figure 8g). The distribution of wind shear in Dandong and precipitation in Lhasa, respectively, can be seen to have influenced the location of local wave sources, thereby affecting the trend of the wave propagation direction in autumn. In winter, the precipitation at Dandong is low whereas the wind shear is strong; hence, the local AGWs are more possibly triggered by wind shear. 91.4% of tracked sources are located east of the Dandong station (Figure 9d), resulting in the dominant southwestward propagation. At Lhasa, AGW events with sources traced locally below 13 km altitude are attributed to the nearby strong wind shear because precipitation in winter is rare. However, the locations of the sources cannot explain the southeastward propagation trend. Considering that the AGWs over Lhasa have shorter wavelengths and lower relative intensities, secondary waves generated by wave breaking or waves forced by conduction are potential causes of the trend. Further investigations are required to reveal the southeastward propagation trend in winter over Lhasa. The different geographical and climatic conditions endow Dandong and Lhasa with distinct characteristics in their local AGW events. Dandong features a temperate humid monsoon climate, characterized by frequent severe convective weather in summer and pronounced wind shear during cold frontal passages in winter. In contrast, Lhasa exhibits a plateau temperate semi-arid climate, where summer convective precipitation primarily occurs in the afternoon. Consequently, the ASAI rarely detects AGWs triggered by local precipitation. Furthermore, wind shear associated with the plateau jet stream significantly influences the generation and propagation of AGWs.

Besides wind shear, the jet imbalance is another potential source of AGWs. Both modelling studies (Zhang FQ, 2004) and extensive

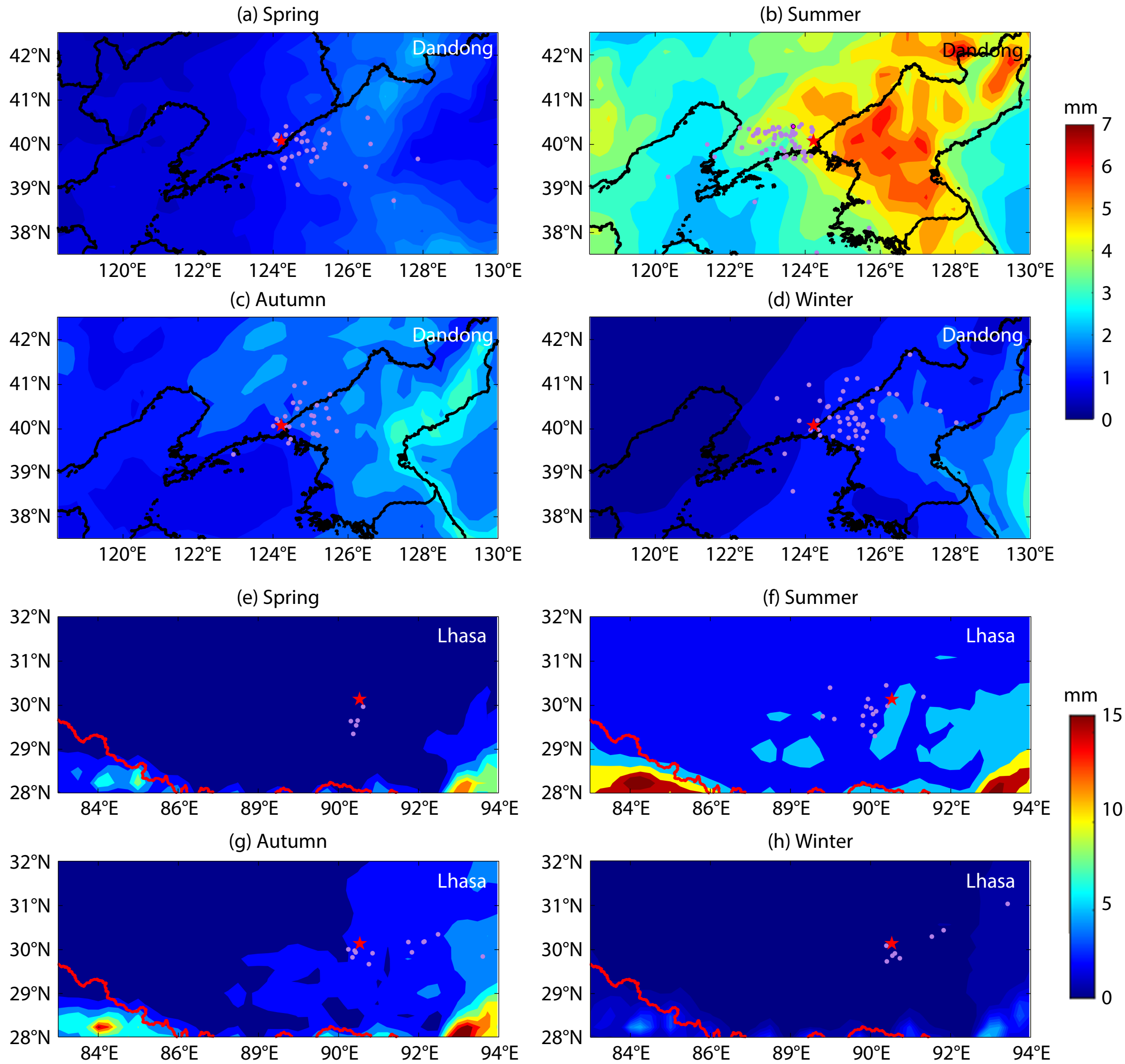

Figure 8. Monthly mean convective precipitation for each season. (a–d) Results for Dandong; (e–h) results for Lhasa. The purple dots indicate the positions of gravity wave sources traced below 13 km, and the red stars represent the locations of the observation stations.

observations (Chun HY et al., 2019) have demonstrated that AGWs excited by jet imbalance typically exhibit mesoscale horizontal wavelengths ranging from 50 to 500 km. Because the wavelengths of AGWs observed at both stations are predominantly below 60 km, the jet imbalance is not discussed as a wave source in this study.

4. Summary

On the basis of 317 AGW events detected by the Dandong station and 202 events recorded by the Lhasa station from 2015 to 2017, we analysed the propagation characteristics and traced the seasonal wave sources, respectively. At the Dandong station, the observed AGWs have horizontal wavelengths mainly in the range of 35–60 km, periods of 14–20 min, speeds of 30–60 m/s, and relative intensities of 0.4–0.6. In contrast, at the Lhasa station, AGWs predominantly range from 15 to 35 km in horizontal wavelength, 4 to 6 min in period, 40 to 100 m/s in speed, and 0.1 to 0.3 in relative intensity. The occurrence rate of AGWs in Dandong shows peaks in both winter and summer, whereas the occurrence rate of AGWs in Lhasa shows peaks only in winter. Tracing the wave sources reveals that the absence of a peak occurrence in summer is due to most AGW events in summer being caused by convective weather and Lhasa experiencing fewer strong convective rain events.

The wind field filtering effect has a substantial impact on the propagation direction of the AGWs, which can explain the northeastward propagation trend of AGWs at the Dandong and Lhasa stations in summer and the mainly southwestward propagation at the Dandong station in winter. In winter, only a few AGWs can be traced to near Lhasa, and the wind field-filtering effect cannot explain the southeastward propagation. These southeastward-propagating waves may originate from secondary waves generated by wave breaking or waves forced by conduction. Further research is needed to verify this issue.

Acknowledgments

This study was supported by the National Key Research and Development Program of China (Grant No. 2022YFF0711402) and the Specialized Research Fund for State Key Laboratories. We

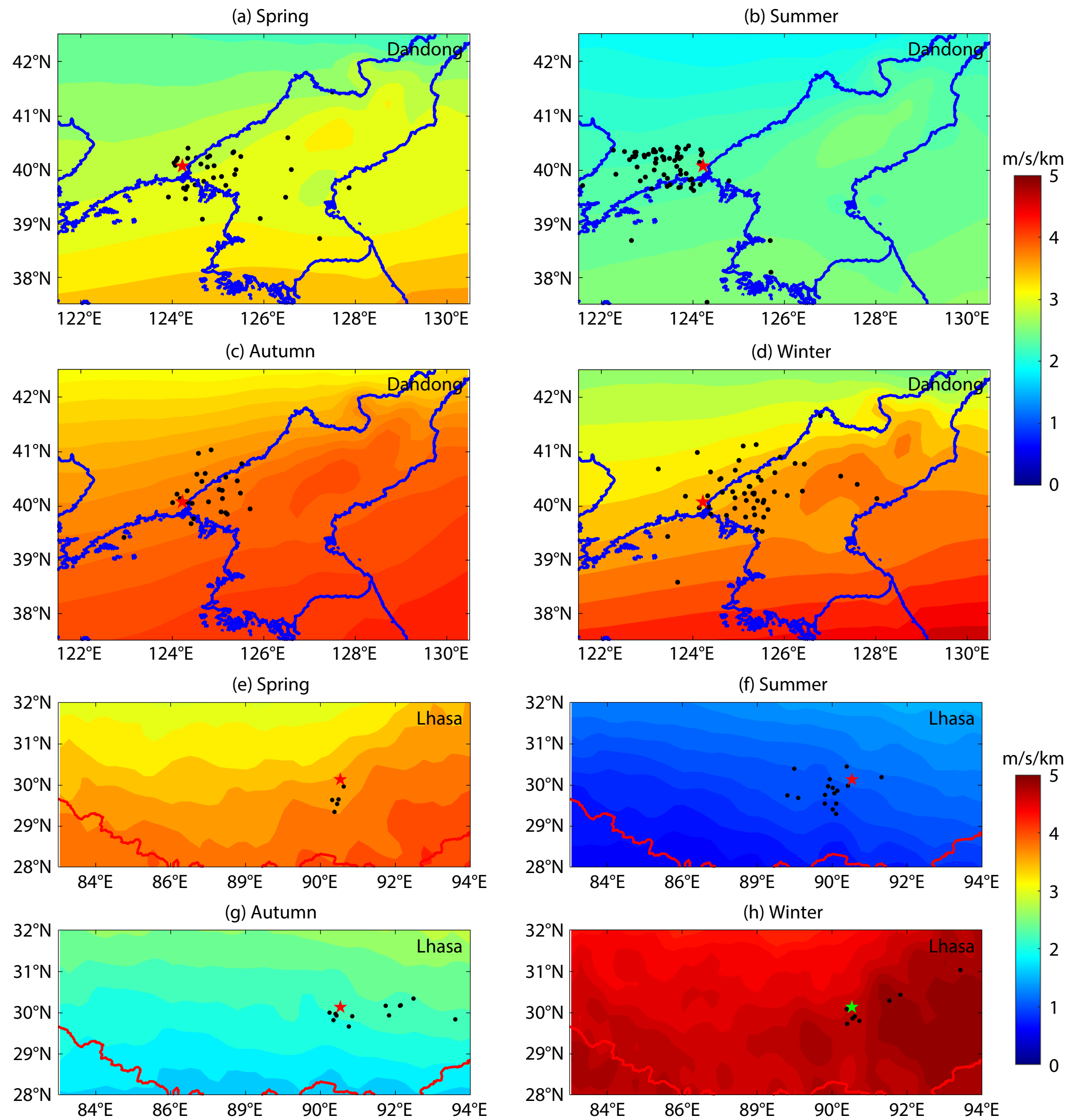

Figure 9. Average vertical wind shear intensity below 13 km. (a–d) Results for Dandong; (e–h) results for Lhasa. The black dots indicate the positions of gravity wave sources traced below 13 km, and the stars represent the observation stations.

acknowledge the use of data from the Chinese Meridian Project. The ECMWF reanalysis data used in this study were obtained from the Copernicus Climate Data Store, including the ERA-5 monthly means for pressure levels (https://cds.climate.copernicus.eu/datasets/reanalysis-era5-pressure-levels-monthly-means) and the ERA-5 daily statistics on single levels (https://cds.climate.copernicus.eu/datasets/derived-era5-single-levels-daily-statistics). The MERRA-2 data were obtained from the NASA Global Modeling and Assimilation Office (GMAO, https://gmao.gsfc.nasa.gov/reanalysis/MERRA-2/).

References

Alexander, M. J., and Teitelbaum, H. (2011). Three-dimensional properties of Andes mountain waves observed by satellite: A case study. *J. Geophys. Res.: Atmos.*, *116*(D23), D23110. https://doi.org/10.1029/2011JD016151

Bramberger, M., Dörnbrack, A., Bossert, K., Ehard, B., Kaifler, B., Mallaun, C., Orr, A., Pautet, P. D., Rapp, M., … Witschas, B. (2017). Does strong tropospheric forcing cause large-amplitude mesospheric gravity waves? A DEEPWAVE case study. *J. Geophys. Res.: Atmos.*, *122*(21), 11422–11443. https://doi.org/10.1002/2017JD027371

Cao, B., and Liu, A. Z. (2022). Statistical characteristics of high-frequency gravity waves observed by an airglow imager at Andes Lidar Observatory. *Earth Space Sci.*, *9*(6), e2022EA002256. https://doi.org/10.1029/2022EA002256

Chun, H. Y., Song, B. G., Shin, S. W., and Kim, Y. H. (2019). Gravity waves associated with jet/front systems. Part I: Diagnostics and their correlations with GWs revealed in high-resolution global analysis data. Asia-Pac. *J. Atmos. Sci.*, *55*(4), 589–608. https://doi.org/10.1007/s13143-019-00104-1

Clemesha, B., and Batista, P. (2008). Gravity waves and wind-shear in the MLT at 23°S. *Adv. Space Res.*, *41*(9), 1472–1477. https://doi.org/10.1016/j.asr.2007.03.085

Dou, X. K., Li, T., Tang, Y. H., Yue, J., Nakamura, T., Xue, X. H., Williams, B. P., and She, C. Y. (2010). Variability of gravity wave occurrence frequency and propagation direction in the upper mesosphere observed by the OH imager in Northern Colorado. *J. Atmos. Sol.-Terr. Phys.*, *72*(5-6), 457–462. https://doi.org/10.1016/j.jastp.2010.01.002

Fritts, D. C., and Luo, Z. G. (1992). Gravity wave excitation by geostrophic adjustment of the jet stream. Part I: Two-dimensional forcing. *J. Atmos. Sci.*, *49*(8), 681–697. https://doi.org/10.1175/1520-0469(1992)049<0681:GWEBGA>2.0.CO;2

Fritts, D. C., and Alexander, M. J. (2003). Gravity wave dynamics and effects in the middle atmosphere. *Rev. Geophys.*, *41*(1), 1003. https://doi.org/10.1029/2001RG000106

Fu, Y. F., Ma, Y. M., Zhong, L., Yang, Y. J., Guo, X. L., Wang, C. H., Xu, X. F., Yang, K., Xu, X. D., … Wang, D. (2020). Land-surface processes and summer-cloud-precipitation characteristics in the Tibetan Plateau and their effects on downstream weather: A review and perspective. *Natl. Sci. Rev.*, *7*(3), 500–515. https://doi.org/10.1093/nsr/nwz226

Garcia, F. J., Taylor, M. J., and Kelley, M. C. (1997). Two-dimensional spectral analysis of mesospheric airglow image data. *Appl. Opt.*, *36*(29), 7374–7385. https://doi.org/10.1364/AO.36.007374

Giongo, G. A., Bageston, J. V., Figueiredo, C. A. O. B., Wrasse, C. M., Kam, H., Kim, Y. H., and Schuch, N. J. (2020). Gravity wave investigations over Comandante Ferraz Antarctic station in 2017: General characteristics, wind filtering and case study. *Atmosphere*, *11*(8), 880. https://doi.org/10.3390/atmos11080880

Hedin, A. E., Fleming, E. L., Manson, A. H., Schmidlin, F. J., Avery, S. K., Clark, R. R., Franke, S. J., Fraser, G. J., Tsuda, T., Vial, F., … Vincent, R. A. (1996). Empirical wind model for the upper, middle and lower atmosphere. *J. Atmos. Terr. Phys.*, *58*(13), 1421–1447. https://doi.org/10.1016/0021-9169(95)00122-0

Jana, S., Rakshit, G., and Maitra, A. (2020). Gravity wave activities associated with convective phenomena at a tropical location near land-sea boundary. *Radio Sci.*, *55*(1), e2019RS006952. https://doi.org/10.1029/2019RS006952

Jiang, J. H., Wu, D. L., and Eckermann, S. D. (2002). Upper Atmosphere Research Satellite (UARS) MLS observation of mountain waves over the Andes. *J. Geophys. Res.: Atmos.*, *107*(D20), 8273. https://doi.org/10.1029/2002JD002091

Kalisch, S., Chun, H. Y., Ern, M., Preusse, P., Trinh, Q. T., Eckermann, S. D., and Riese, M. (2016). Comparison of simulated and observed convective gravity waves. *J. Geophys. Res.: Atmos.*, *121*(22), 13474–13492. https://doi.org/10.1002/2016JD025235

Kim, Y. H., Lee, C. S., Chung, J. K., Kim, J. H., and Chun, H. Y. (2010). Seasonal variations of mesospheric gravity waves observed with an airglow all-sky camera at Mt. Bohyun, Korea (36° N). *J. Astron. Space Sci.*, *27*(3), 181–188. https://doi.org/10.5140/JASS.2010.27.3.181

Lai, C., Xu, J. Y., Yue, J., Yuan, W., Liu, X., Li, W., and Li, Q. Z. (2019). Automatic extraction of gravity waves from all-sky airglow image based on machine learning. *Remote Sens.*, *11*(13), 1516. https://doi.org/10.3390/rs11131516

Li, Q., Xu, J., Yue, J., Yuan, W., and Liu, X. (2011). Statistical characteristics of gravity wave activities observed by an OH airglow imager at Xinglong, in northern China. *Ann. Geophys.*, *29*(8), 1401–1410. https://doi.org/10.5194/angeo-29-1401-2011

Li, Q. Z., Xu, J. Y., Liu, X., Yuan, W., and Chen, J. S. (2016). Characteristics of mesospheric gravity waves over the southeastern Tibetan Plateau region. *J. Geophys. Res.: Space Phys.*, *121*(9), 9204–9221. https://doi.org/10.1002/2016JA022823

Li, Q. Z., Yusupov, K., Akchurin, A., Yuan, W., Liu, X., and Xu, J. Y. (2018). First OH airglow observation of mesospheric gravity waves over European Russia region. *J. Geoohys. Res.: Space Phys.*, *123*(3), 2168–2180. https://doi.org/10.1002/2017JA025081

Li, Q. Z., Xu, J. Y., Gusman, A. R., Liu, H. L., Yuan, W., Liu, W. J., Zhu, Y. J., and Liu, X. (2024). Upper-atmosphere responses to the 2022 Hunga Tonga–Hunga Ha'apai volcanic eruption via acoustic gravity waves and air–sea interaction. *Atmos. Chem. Phys.*, *24*(14), 8343–8361. https://doi.org/10.5194/acp-24-8343-2024

Lin, Z. S., Wang, Q. Y., and Lai, C. (2023). Analysis of airglow image classification based on feature map visualization. *Appl. Sci.*, *13*(6), 3671. https://doi.org/10.3390/app13063671

Luo, Z. G., and Fritts, D. C. (1993). Gravity-wave excitation by geostrophic adjustment of the jet stream. Part II: Three-dimensional forcing. *J. Atmos. Sci.*, *50*(1), 104–115. https://doi.org/10.1175/1520-0469(1993)050<0104:GWEBGA>2.0.CO;2

Marks, C.J., and Eckermann, S. D. (1995). A three-dimensional nonhydrostatic ray-tracing model for gravity waves: Formulation and preliminary results for the middle atmosphere. *J. Atmos. Sci.*, *52*(11), 1959–1984. https://doi.org/10.1175/1520-0469(1995)052<1959:ATDNRT>2.0.CO;2

Medeiros, A. F., Taylor, M. J., Takahashi, H., Batista, P. P., and Gobbi, D. (2003). An investigation of gravity wave activity in the low-latitude upper mesosphere: Propagation direction and wind filtering. *J. Geophys. Res.: Atmos.*, *108*(D14), 4411. https://doi.org/10.1029/2002JD002593

Medeiros, A. F., Buriti, R. A., Machado, E. A., Takahashi, H., Batista, P. P., Gobbi, D., and Taylor, M. J. (2004). Comparison of gravity wave activity observed by airglow imaging at two different latitudes in Brazil. *J. Atmos. Sol.-Terr. Phys.*, *66*(6-9), 647–654. https://doi.org/10.1016/j.jastp.2004.01.016

Nath, D., and Chen, W. (2013). Investigating the dominant source for the generation of gravity waves during Indian summer monsoon using ground-based measurements. *Adv. Atmos. Sci.*, *30*(1), 153–166. https://doi.org/10.1007/s00376-012-1273-y

Picone, J. M., Hedin, A. E., Drob, D. P., and Aikin, A. C. (2002). NRLMSISE-00 empirical model of the atmosphere: Statistical comparisons and scientific issues. *J. Geophys. Res.: Space Phys.*, *107*(A12), 1468. https://doi.org/10.1029/2002ja009430

Rienecker, M. M., Suarez, M. J., Gelaro, R., Todling, R., Bacmeister, J., Liu, E., Bosilovich, M. G., Schubert, S. D., Takacs, L., … Woollen, J. (2011). MERRA: NASA's modern-era retrospective analysis for research and applications. *J. Climate*, *24*(14), 3624–3648. https://doi.org/10.1175/JCLI-D-11-00015.1

Suzuki, S., Shiokawa, K., Otsuka, Y., Ogawa, T., and Wilkinson, P. (2004). Statistical characteristics of gravity waves observed by an all-sky imager at Darwin, Australia. *J. Geophys. Res.: Atmos.*, *109*(D20), 2003JD004336. https://doi.org/10.1029/2003JD004336

Taylor, M. J., Ryan, E. H., Tuan, T. F., and Edwards, R. (1993). Evidence of preferential directions for gravity wave propagation due to wind filtering in the middle atmosphere. *J. Geophys. Res.: Space Phys.*, *98*(A4), 6047–6057. https://doi.org/10.1029/92JA02604

Taylor, M. J. (1997). A review of advances in imaging techniques for measuring short period gravity waves in the mesosphere and lower thermosphere. *Adv. Space Res.*, *19*(4), 667–676. https://doi.org/10.1016/S0273-1177(97)00161-0

Triplett, C. C., Collins, R. L., Nielsen, K., Harvey, V. L., and Mizutani, K. (2017). Role of wind filtering and unbalanced flow generation in middle atmosphere gravity wave activity at Chatanika Alaska. *Atmosphere*, *8*(2), 27. https://doi.org/10.3390/atmos8020027

Wang, Y., Zhang, L. F., Zhang, Y., and Guan, J. P. (2019). Effects of tropospheric vertical wind shear on gravity waves generated by tropical cyclones. *Geophys. Res. Lett.*, *46*(8), 4523–4530. https://doi.org/10.1029/2019GL082085

Wrasse, C. M., Nakamura, T., Takahashi, H., Medeiros, A. F., Taylor, M. J., Gobbi, D., Denardini, C. M., Fechine, J., Buriti, R. A., … Admiranto, A. G. (2006). Mesospheric gravity waves observed near equatorial and low–middle latitude stations: Wave characteristics and reverse ray tracing results. *Ann. Geophys.*, *24*(12), 3229–3240. https://doi.org/10.5194/angeo-24-3229-2006

Wrasse, C. M., Nyassor, P. K., Da Silva, L. A., Figueiredo, C. A. O. B., Bageston, J. V., Naccarato, K. P., Barros, D., Takahashi, H., and Gobbi, D. (2024). Studies on the propagation dynamics and source mechanism of quasi-monochromatic gravity waves observed over São Martinho da Serra (29° S, 53° W), Brazil. *Atmos. Chem. Phys.*, *24*(9), 5405–5431. https://doi.org/10.5194/acp-24-5405-2024

Xu, J. Y., Li, Q. Z., Yue, J., Hoffmann, L., Straka, W. C., Wang, C. M., Liu, M. H., Yuan, W., Han, S., Miller, S. D., … Ning, B. Q. (2015). Concentric gravity waves over northern China observed by an airglow imager network and satellites. *J. Geophys. Res.: Atmos.*, *120*(21), 11058–11078. https://doi.org/10.1002/2015JD023786

Zhang, F. Q. (2004). Generation of mesoscale gravity waves in upper-tropospheric jet–front systems. *J. Atmos. Sci.*, *61*(4), 440–457. https://doi.org/10.1175/1520-0469(2004)061<0440:GOMGWI>2.0.CO;2